Two-Hundred-Newton Laboratory-Scale Hybrid Rocket Testing for Paraffin Fuel-Performance Characterization

G. D. Di Martino,* S. Mungiguerra,* C. Carmicino,† and R. Savino‡
University of Naples Federico II, 80125 Napoli, Italy
and
D. Cardillo,§ F. Battista,¶ M. Invigorito,** and G. Elia**
Centro Italiano Ricerche Aerospaziali, 81043 Capua, Italy

A series of firing tests have been performed on a laboratory-scale hybrid rocket engine of 200 N class, fed with gaseous oxygen through a converging nozzle injector, to assess the mechanical feasibility and regression rate of a newly developed paraffin-based fuel. Such an injector configuration, by producing recirculation at the motor head hand, has been already demonstrated to influence the standard fuels regression rate, which yields an increase with the port diameter at given mass flux. In this study, paraffin-fuel regression rate dependence on the mass flux and grain port diameter in the form of a power function is determined to be similar to that established with polymeric fuels, despite the different mechanism of consumption that involves the fuel surface liquid-layer instability other than the vaporization typical of classical polymers. Comparison with some data in the literature is presented. Data retrieved from the testing campaign are compared with numerical results obtained by adopting a simple but efficient modeling strategy and a commercial solver. The numerical solution gives evidence of the recirculating flow at the injector exit, which is also responsible for the paraffin contamination observed in the motor prechamber. A good agreement is found with chamber pressure experimentally measured.

Nomenclature

A_t	=	nozzle throat area, m^2
a	=	regression rate factor
B	=	blowing number
C^*	=	theoretical characteristic exhaust velocity, m/s
c_p	=	gas specific heat at constant pressure, $J/(kg \cdot K)$
D	=	fuel grain port diameter, mm
d_{inj}	=	injector exit diameter, mm
e	=	specific internal energy, J/kg
e_0	=	specific total energy, J/kg
G	=	mass flux, $kg/(m^2 \cdot s)$
k	=	turbulent kinetic energy, m^2/s^2
L	=	fuel grain length, mm
M_w	=	molecular weight, kg/mol
m	=	diameter/chamber pressure exponent
$\dot{m}$	=	mass flow rate, kg/s
n	=	oxidizer mass flux exponent
OF	=	oxidizer-to-fuel ratio
Pr	=	Prandtl number
p	=	pressure, Pa
q	=	heat flux, W/m^2
R	=	universal gas constant, $J/(K \cdot mol)$
R^2	=	squared correlation factor
Re_D	=	Reynolds number based on port diameter
$\dot{r}$	=	fuel regression rate, mm/s
St	=	Stanton number
T	=	temperature, K
Th	=	thrust, N
t	=	time, s
t_b	=	burning time, s
u	=	gas velocity, m/s
X	=	species molar fraction
x	=	generic coordinate, m
Y	=	species mass fraction
y^+	=	dimensionless wall distance
ΔM	=	fuel mass loss, kg
η	=	combustion efficiency
λ	=	gas molecular thermal conductivity, $W/(m \cdot s)$
μ	=	gas molecular viscosity, $kg/(m \cdot s)$
ρ	=	gas density, kg/m^3
τ	=	stress tensor, $kg/(m \cdot s^2)$
ω	=	turbulence specific dissipation rate, 1/s

Subscripts

c	=	chamber
f	=	fuel
ox	=	oxidizer
1	=	initial
2	=	final

Superscripts

~	=	time average
—	=	time-space average

*Ph.D. Student, Department of Industrial Engineering, Aerospace Division, P.le Tecchio 80.

†Research Consultant, Department of Industrial Engineering, Aerospace Division, P.le Tecchio 80.

‡Professor, Department of Industrial Engineering, Aerospace Division, P.le Tecchio 80.

§Research Engineer, Methodologies and Technologies for Space Propulsion Laboratory, Via Maiorise.

¶Head, Methodologies and Technologies for Space Propulsion Laboratory, Via Maiorise.

**Research Engineer, Propulsion Test Facilities, Via Maiorise.

I. Introduction

WHEN dealing with hybrid rockets, one cannot avoid stating that this chemical propulsion technology presents several considerable advantages with respect to solid and liquid propellant rockets, such as the intrinsic safety, lower development costs, and minimal environmental impact, while still providing the reignition and throttling capability of liquid engines along with a higher specific

impulse than solid propellants, as well as a density impulse better than liquids [1]. All of the aforementioned characteristics stem from the basic system configuration in which propellants are combined in separate phases (i.e., the oxidizer is stored in tanks in the liquid state, or gaseous in rare cases, and it is properly injected in the combustion chamber where the solid fuel grain is bonded).

Practical application of hybrid thrusters is, however, still hindered probably for the low fuel regression rate compared to solid rockets [2,3]. In particular, for conventional polymeric fuels, such as polyethylene and hydroxyl-terminated polybutadiene (HTPB), the burn rate is limited by the diffusion processes occurring in the boundary layer developing on the solid-fuel surface, and by the reduction of the heat transfer from the flame zone caused by gas blowing from the fuel surface [4]. Several strategies have been suggested to mitigate this shortcoming, such as, among the most common ones, the design of multiport grains for which, despite the slow regression, a high thrust level can be obtained; the design of injection systems inducing recirculating [5,6] or swirling oxidizer flows [7,8]; and the addition of metal additives or solid particles, which mostly raise the density impulse with a minor effectiveness on the regression rate [9]. Yet all of these methods lead to an increase of the system complexity and associated cost without producing major improvements of the engine overall performance [10].

In this scenario, substantial interest has been focused on the paraffin-based fuels as enhancers of regression rate for the different mechanisms involved in the fuel surface/gaseous flow interaction [11]. As widely recognized, with this class of materials, known as liquefying fuels, in addition to the classical fuel gasification, for the formation of a low-viscosity unstable melt layer on the burning surface, fuel liquid droplets are entrained into the main gas stream [12,13], which largely increases the solid regression rate. As a result, the overall regression rate can be considered composed by two fractions, one determined by classical fuel vaporization and the other by the liquid entrainment. This phenomenon is caused by the superficial liquid-layer instability, which is strongly affected by the fuel composition and its thermomechanical properties [14]. As a consequence, the behavior of paraffin-based fuels can significantly change depending on the specific fuel formulation, the manufacturing process, and the motor operating conditions. Mechanical tests of paraffin wax have shown that this fuel is a brittle, low-strength material, yielding a high risk of failure under severe launch loading conditions. Thus, mechanical strengtheners have been identified, which can be added to improve the structural performance of the fuel grains; but additives alter the fuel liquid viscosity and reduce the effect of entrainment regression, producing a major impact on motor performance that needs to be assessed. This is the reason that nonnegligibly different fuel performance is often observed in the literature [15]. For instance, in a previous testing campaign conducted on the same small-scale motor adopted in the present work but burning gaseous nitrous oxide [16], paraffin fuel formulations were studied to improve the poor mechanical stiffness with the addition of 15% by weight styrene–ethylene–butylene–styrene (SEBS) copolymer and 1% carbon black, and the casting temperature was found to have a significant impact on the grain structural strength.

Moreover, with liquefying fuels, the classical theories (starting from the famous work of Marxman et al. [4,17]), elaborated to predict the regression rate of standard fuels, are no longer valid, whereas the analytical models specifically developed (such as the one in Ref. [18]) are based on semi-empirical equations.

Dedicated testing is, hence, needed for the prediction of the engine performance and to support the design of full scale rockets. Usually, experimental data available in the literature are correlated to express the regression rate as a function of the oxidizer mass flux only, thus neglecting the effect of other significant operating parameters, which can have a role in the interaction between the gas stream and the fuel grain consumption mechanism.

In fact, on the one hand, looking at the effect of the modifications of heat transfer to fuel surface, in previous works it has been shown that the regression rate of classical polymeric fuels is influenced by the arrangement of the oxidizer injector [5,6]. For instance, when a conical axial injector is employed, the motor internal ballistics is governed by the recirculation zone induced by the oxidizer jet discharged from the injector into the solid fuel port [19]. The ensuing flowfield is typical of reattaching regions, and the resulting heat transfer to the wall depends on the fuel port-to-injector diameter ratio. The macroscopic result is that the fuel regression rate is directly influenced by the port diameter other than by the mass flux [9,19] in such a way as it increases with the port diameter at constant mass flux. On the other hand, looking at the characteristic time scales of diffusion and chemistry, it is generally accepted that the regression rate of polymeric fuels is independent from the chamber pressure in a wide range of oxidizer mass fluxes, whereas it has an impact when mass flux is very large and chemical kinetics begins to be slower than diffusion [20,21]. The influence of the aforementioned parameters has not yet been investigated with paraffin-based fuels, for which only the vaporization fraction of regression rate is determined by the surface heat flux, whereas the remaining entrainment fraction essentially depends on the dynamic pressure and melt-layer thickness as well as on the fuel liquid viscosity and surface tension at the characteristic temperature of the layer. Therefore, compared to classical fuels, the flow recirculation at the grain inlet and the chamber pressure are expected to have different effects.

In this work, a firing test campaign has been carried out with the laboratory small-scale rocket used in Ref. [16] burning the SASOL 0907 paraffin-based fuel, with gaseous oxygen. The main objective of the firing test activity is to address the mechanical behavior of the paraffin grains in the severe combustion chamber conditions, although no polymeric additives have been included, and to fully characterize the regression rate performance. The employment of a conical subsonic nozzle injector for the gaseous oxygen allowed the investigation of the effect of a recirculating flow pattern on the consumption also for this new class of fuels. Moreover, the influence of the chamber pressure on the performance has been analyzed and extensively discussed.

A simple but efficient computational fluid dynamics (CFD) model has been employed to support the firing test, giving insight on the thermofluid dynamic flowfield developed in the combustion chamber of the engine and providing additional useful information that is not experimentally measurable, such as the temperature distribution and the heat fluxes achieved on the different engine components. The aim is also to develop a performance database useful for the design, development, and test of a larger paraffin-based 1-kN-class hybrid rocket demonstrator, which represents the next step of the current research project.

II. Experimental Setup and Data Reduction Technique

A. Lab-Scaled Rocket and Test Facility

The lab-scale rocket, the experimental test facility, and the data reduction methodology used in the present investigation are described in this section. The test facility is a versatile experimental setup primarily designed for firing hybrid rocket engines of several sizes [16]. The equipment includes a test rig and a general-purpose data acquisition system, which allow performing several types of tests.

Figure 1 shows the piping and instrumentation schematic of the test rig. Gaseous oxygen is supplied by a reservoir of four cylinders; pressure regulators set the operating pressure along the motor feed line. Oxygen mass flow rate is evaluated through gas temperature and pressure measurements upstream of the throat of a chocked Venturi tube. Nitrogen is purged into the chamber for the burnout and in case of an emergency shutdown.

The 200-N-class hybrid rocket employed in this study is depicted in Fig. 2.

The rocket has an axisymmetric combustion chamber, with 350 mm length and 69 mm case inner diameter. The motor forward closure accommodates a converging nozzle injector whose exit-section diameter is 6 mm.

Upstream and downstream of the solid grain, a dump plenum (25 mm long and with 44 mm inner diameter) and an aft-mixing chamber (58 mm long and with 45 mm inner diameter) are set up,
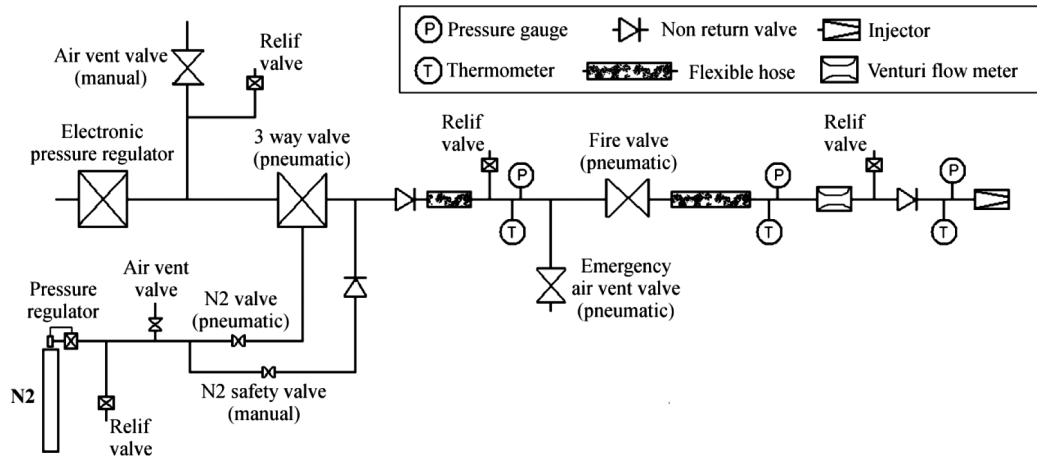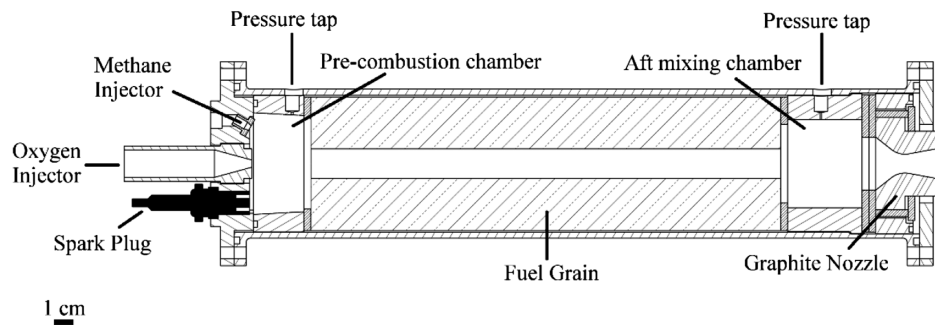
Fig. 1   Test facility schematic.

Fig. 2   Motor layout.

respectively. A graphite converging–diverging nozzle with 10.6 mm throat diameter and an area expansion ratio equal to 2.45 has been employed. No significant throat erosion has been detected after the firing tests.

The equipment allows the full automation of the motor ignition, the firing test execution, and the measurement of significant data during the test. In particular, the engine ignition is realized injecting, in the early moments of the test, a small amount of methane simultaneously with the prescribed oxygen mass flow rate. In this way, the two gases mix in the prechamber where a spark plug, powered by a Honeywell solid-state igniter spark generator, is arranged. This process ensures repeatable ignition conditions. Chamber pressure is measured with two Setra C206 transducers, which are set up in the prechamber and in the aft mixing chamber. Furthermore, the rocket is supported on the test bench with four load cells, which allow evaluating the motor thrust by computing the sum of the loads measured with each cell. The analog signals generated by thermocouples, pressure transducers, and load cells are sampled at 5 kHz, digitally converted, processed, and recorded on the hard disk by a National Instruments PXI Express standard system interconnected with the computer by means of fiber optic connections. All the signals are stored in a binary format for postprocessing and, after downsampling the data to 100 Hz with a boxcar average, in text format. All diagrams in the forthcoming sections will show downsampled data.

B.   Paraffin Grains Manufacturing

Cylindrical single-port paraffin-based fuel grains were manufactured by melting the wax and pouring it in a steel cylindrical mold, where it is cooled and solidified by a temperature-controlled process, in such a way that the solidification process is rather uniform and the formation of internal bubbles or weakness is avoided. According to the dimension of the hybrid rocket components described in Sec. II. A, paraffin cylinders with a length of 220 mm and an outer diameter of 69 mm have been realized. Finally, the central port with the chosen initial diameter is realized with a turning machine.

The main component of the fuel investigated in this work is the microcrystalline paraffin wax commercialized by SASOL, labeled with the trade code 0907. As shown in Ref. [22], this paraffin wax was selected for its high fracture toughness and workability deriving from its characteristic property of forming microcrystals. In Table 1, the physical-chemical properties of the SASOL 0907, as declared by the supplier, are reported. Other thermophysical and rheological properties of this paraffin are discussed in [22,23].

The typical black color of the paraffin grains is obtained adding to the melted wax a small amount of a blackening additive, which is expected to increase the thermal radiation absorption at the fuel surface improving the regression rate (Refs. [10,12]).

No polymeric additives have been included in the formulation to avoid a worsening effect on the fuel regression rate.

C.   Test Matrix Definition

The test matrix is reported in Table 2. Nominal test settings for the experimental campaign, along with the estimation of the corresponding average parameters, are shown. Initial port diameter, burning time, and oxygen mass flow rate have been selected, according to the facility constraints, to achieve average oxidizer mass fluxes in the range of about 40 kg/(m^2 · s) up to values above 100 kg/(m^2 · s), with regression rate varying between about 1.4 and 2.8 mm/s and average port diameters roughly in three bins: 21–24, 25–26, and 27–30 mm.

Because the regression rate is an unknown parameter to be measured, and the average oxidizer mass flux and chamber pressure

Table 1   SASOL 0907 paraffin wax properties (as declared by the supplier)

Melting or dropping point	Congealing point	Oil content	Penetration at 25°C (1/10)
88–102°C	83–94°C	0–1.5%	4–10 mm

Table 2　Test matrix

Test	Nominal test settings			Expected parameters calculated with the regression rate law reported in [24]				Expected parameters calculated with the regression rate law reported in [25]			
	D_1, mm	$\dot{m}_{ox}$, g/s	t_b, s	$\bar{D}$, mm	$\bar{G}_{ox}$, kg/(m²·s)	$\bar{r}$, mm/s	p_c, bar	$\bar{D}$, mm	$\bar{G}_{ox}$, kg/(m²·s)	$\bar{r}$, mm/s	p_c, bar
0a	15	20	5	21.9	53.3	1.37	5.9	23.4	46.5	1.68	6.3
0b	15	25	5	22.6	62.5	1.51	7.4	24.2	54.3	1.84	7.7
1	15	15	5	21.0	43.2	1.20	4.5	22.4	37.9	1.49	5.0
2	15	25	5	22.6	62.5	1.51	7.4	24.2	54.3	1.84	7.7
3	15	30	5	23.2	71.1	1.64	9.1	24.9	61.5	1.99	9.1
4	15	40	5	24.2	86.7	1.85	12.3	26.1	74.6	2.23	11.8
5	15	30	5	23.2	71.1	1.64	9.1	24.9	61.5	1.99	9.1
6	15	40	5	24.2	86.7	1.85	12.3	26.1	74.6	2.23	11.8
7	20	40	5	27.8	65.8	1.56	12.3	29.6	58.1	1.92	11.8
8	20	45	4	27.0	78.7	1.75	13.9	28.6	70.0	2.15	13.4
9	20	50	4	27.3	85.2	1.84	15.4	29.0	75.6	2.25	15.0
10	20	55	4	27.7	91.5	1.92	16.9	29.4	81.1	2.35	16.7
11	20	60	4	28	97.6	2.00	18.4	29.8	86.3	2.44	18.3
12	15	60	4	24.4	128.1	2.36	18.5	26.3	110.6	2.82	18.3
1W	15	40	5	24.2	86.7	1.85	12.32	26.1	74.6	2.23	11.8
2W	15	60	4	24.4	128.1	2.36	18.5	26.3	110.6	2.82	18.3
∗ (paraffin plus additives)	20	30	4	——	——	——	——	——	——	——	——

depend on the regression rate, the expected data were estimated assuming the classical regression rate law:

$$\dot{r} = aG_{ox}^n \qquad (1)$$

where the coefficients a and n have been selected from the values available in literature relevant to the combustion of gaseous oxygen with paraffin-based fuels; two sets have been considered: the one reported by Karabeyoglu et al. in [24] and the one found by Evans et al. in [25]. Integrating Eq. (1) from the initial diameter for the nominal test duration, the space-averaged final port diameter $\tilde{D}_2$ and, consequently, the time-space-averaged port diameter $\bar{D}$ can be calculated. Then, considering the prescribed oxidizer mass flow rate, the average oxidizer mass flux $\bar{G}_{ox}$ and the corresponding average regression rate $\bar{r}$ can be estimated. The average fuel mass flow rate can be easily calculated as

$$\bar{\dot{m}}_f = \rho_f \pi \bar{D} L \bar{r} \qquad (2)$$

where ρ_f is the solid fuel density, and L is the length of the grain, and correspondingly the average mixture ratio $\overline{OF} = (\dot{m}_{ox}/\bar{\dot{m}}_f)$ can be derived. From these calculations, a first estimation of the aft-chamber pressure p_c can be performed by means of an iterative procedure to solve the steady-state mass balance equation:

$$\frac{\dot{m}_{ox}}{A_t}\left(1 + \frac{1}{\overline{OF}}\right) = \frac{p_c}{\eta \bar{C}^*} \qquad (3)$$

in which A_t is the nozzle throat area, $\bar{C}^*$ is the theoretical characteristic exhaust velocity (that primarily depends on the mixture ratio and, to a minor degree, on pressure), and the combustion efficiency η has been assumed equal to unity. For the dependence of the C^* on pressure, Eq. (3) is implicit, and an iterative calculation technique is needed. A combustion pressure is first assumed, and then the CEA chemical equilibrium code [26] developed by NASA is run to calculate the equilibrium composition and the theoretical exhaust velocity, assuming frozen flow through the nozzle, at the given OF ratio in input. Finally, combustion pressure is adjusted repeatedly until convergence.

Notice that, although for most of the tests an initial port diameter equal to 15 mm has been chosen, for tests 7 through 11 it has been set equal to 20 mm, to get higher values of the chamber pressure for a fixed oxidizer mass flux.

For the tests with higher oxidizer mass flow rate (tests 8 through 12) the burning duration has been set to 4 s to obtain higher values of the average oxidizer mass flux.

With these settings, all the parameters are expected to range significantly to draw conclusions on the regression rate dependency upon mass flux and port diameter and achieve widely different combustion chamber pressures to assess the numerical results.

Finally, paraffin grains of tests 1 W and 2 W have been casted without the addition of the blackening additive, with the purpose of seeing if any difference in the fuel behavior arises. Whereas, in analogy with the investigation in Ref. [16], polymeric additives (30% by weight SEBS in this case) have been included in the paraffin grain of test ∗.

D.　Firing Data Reduction Technique

The main parameters directly measured in the firing tests are the oxidizer mass flow rate $\dot{m}_{ox}$, chamber pressure p_c, motor thrust Th, fuel grain mass consumption ΔM, and the burning time t_b. The remaining quantities of interest can be derived from the measured ones. From the fuel grain mass loss and the operation time, the average fuel mass flow rate can be calculated as

$$\bar{\dot{m}}_f = \frac{\Delta M}{t_b} \qquad (4)$$

The space-averaged final port diameter can be calculated from the mass loss as

$$\tilde{D}_2 = \sqrt{D_1^2 + \frac{4}{\pi}\frac{\Delta M}{\rho_f L}} \qquad (5)$$

where D_1 and L are the grain initial diameter and length, respectively. The time-space-averaged port diameter can be then evaluated as

$$\bar{D} = \frac{D_1 + \tilde{D}_2}{2} \qquad (6)$$

and the average oxidizer mass flux can be calculated as

$$\bar{G}_{ox} = \frac{4\bar{\dot{m}}_{ox}}{\pi \bar{D}^2} \qquad (7)$$

Finally, the time-space-averaged fuel regression rate can be evaluated as

$$\bar{r} = \frac{\tilde{D}_2 - D_1}{2t_b} \qquad (8)$$

The main factors of uncertainty involving the measured quantities are the determination of the burning duration (i.e., the time interval
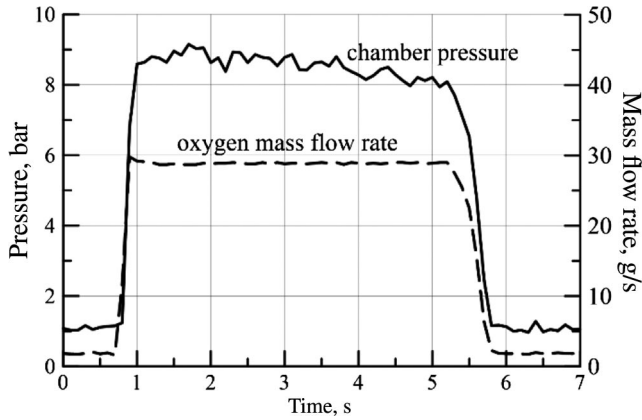
Fig. 3 Chamber pressure and oxygen mass flow rate measured during firing test 3.

between the inflection point on the pressure rise branch at the motor startup and the one on the pressure drop at the burnout); the dispersion of the grain port initial diameter measurements; and of course, to a lesser degree, the scale sensitivity for the measurement of the initial and final grain masses and the signal oscillations during the test in the measurement of the oxidizer mass flow rate. For the details of the uncertainty assessment procedure, refer to [9].

III. Experimental Results on the Subscale Hybrid Engine

The typical test sequence is described here, considering test 3 as an example. Figure 3 shows the typical evolution of the motor chamber pressure over the firing, along with the oxygen mass flow rate. The oxygen feeding valve starts to open at 0.0 s (test initial time) to deliver the oxygen flow rate targeted for the test (about 30 g/s in this case), but for the valve opening delay, oxygen starts flowing after about 0.7 s. In the meanwhile, methane is injected into the chamber and the spark plug is activated, so that ignition takes place just 0.1 s after the oxygen injection, and the chamber pressure starts to rise. The oxygen valve starts to close when the set test duration is elapsed (5 s in this case) plus about 0.4 s lag, and it is completely closed after about 0.8 s; simultaneously, high-pressure nitrogen is fed to the chamber for immediate shutdown.

Table 3 summarizes the main experimental parameters measured over the firing tests as explained in Sec. II.D.

The average oxidizer mass flow rate as well as the average pressure and motor thrust over the firing have been determined by averaging the instantaneous values over the burning time.

Figure 4 shows the measured values of the regression rate as a function of the average oxidizer mass flux, compared with some data available in the literature. With respect to the regression rate trends assumed to define the test matrix, it can be noticed that the experimental points at lower oxidizer mass flux fall in between the curves obtained by Karabeyoglu et al. [24] and Evans et al. [25]. At higher values of the oxidizer mass flux, regression rate points are closer to the curve defined by Evans. The regression rate obtained with the grain of paraffin casted with polymeric additives is definitely lower. If one considers regression rate depending on the oxygen mass flux alone, the following regression rate power law is obtained with a best fit of the data relative to all the tests performed except for test 2 and test $*$:

$$\dot{r} = aG_{ox}^n \quad a = 0.071; \quad n = 0.795 \quad (R^2 = 0.922) \quad (9)$$

in which the regression rate is expressed in millimeters per second, and the mass flux in kilograms per square meter second. However, data appear scattered in the regression rate/mass flux plane; they have been, then, reorganized and grouped in three sets based on the average port diameter in the test (see Fig. 4) to assess the effect of the port diameter itself.

With the aim of interpreting the data shown previously and eventually presenting a physical basis for the correlations discussed later, the heat transfer model developed in Ref. [5] is shortly recalled here for the sake of convenience.

Assuming that the driving factor of fuel regression is the convective heat transfer to the wall, starting from the model developed by Marxman and Gilbert [4], it can be easily demonstrated that

$$\rho_f \dot{r}/G = 0.023 Re_D^{-0.2} Pr^{-(2/3)}(St_j/St_0)B \quad (10)$$

where St_j is the Stanton number in the actual flowfield affected by the injection effects in the presence of wall blowing, and $St_0 = 0.023 Re_D^{-0.2} Pr^{-2/3}$ is the classical Stanton number in an equivalent (i.e., with equal mass flux) turbulent fully developed pipe flow without wall blowing. Note that the subscript 0 refers to the condition with no blowing from the wall. To isolate the effects of the oxidizer injection pattern on the flowfield in the port, the Stanton number ratio can be further manipulated as follows:

$$St_j/St_0 = (St_j/St_{0j})(St_{0j}/St_0) \quad (11)$$

where St_{0j} is the Stanton number corresponding to the flowfield affected by the injection effects without wall blowing; thus, the term

Table 3 Experimental test results

| Test	Effective oxygen mass flow rate, g/s	Effective burning time, s	Time-space-averaged port diameter, mm	Average oxidizer mass flux, kg/(m² · s)	Average regression rate, mm/s	Average overall mixture ratio	Average chamber pressure, bar	Average thrust, N
0a	19.1 ± 1.2	4.2 ± 0.25	21.7 ± 0.1	51.88 ± 3.73	1.58 ± 0.15	0.8 ± 0.12	4.5	39
0b	26 ± 0.08	5.6 ± 0.14	24.6 ± 1.75	54.50 ± 7.8	1.74 ± 0.4	4.16 ± 0.8	7.0	63
1	16 ± 0.06	3.5 ± 0.14	20.5 ± 0.29	48.38 ± 1.54	1.63 ± 0.22	0.77 ± 0.1	4.9	39
2	25 ± 0.35	4.7 ± 0.2	25.1 ± 0.44	50.52 ± 2.43	2.15 ± 0.24	0.74 ± 0.09	8.0	73
3	29 ± 0.13	4.8 ± 0.17	23.6 ± 0.23	66.26 ± 1.59	1.80 ± 0.16	1.04 ± 0.1	8.5	82
4	39 ± 0.27	4.9 ± 0.15	25.3 ± 0.3	77.11 ± 2.32	2.08 ± 0.17	1.17 ± 0.1	11.5	118
5	29 ± 0.68	5.4 ± 0.14	25.0 ± 0.06	59.22 ± 1.66	1.79 ± 0.1	1.03 ± 0.07	8.0	80
6	38 ± 0.85	5.6 ± 0.17	26.6 ± 0.16	67.83 ± 2.3	2.04 ± 0.13	1.10 ± 0.09	11.2	114
7	38 ± 0.85	5.1 ± 0.15	29.3 ± 0.14	56.28 ± 1.77	1.83 ± 0.12	1.13 ± 0.09	11.1	112
8	44 ± 0.75	4 ± 0.15	28.5 ± 0.21	68.88 ± 2.17	2.11 ± 0.16	1.16 ± 0.11	13.2	136
9	50.2 ± 1.07	4 ± 0.16	29.0 ± 0.12	75.90 ± 2.23	2.28 ± 0.17	1.20 ± 0.11	15.7	162
10	55.5 ± 1.36	3.8 ± 0.16	29.0 ± 0.04	83.75 ± 2.26	2.41 ± 0.17	1.26 ± 0.11	16.9	178
11	60 ± 1.59	3.9 ± 0.22	29.9 ± 0.02	85.23 ± 2.13	2.6 ± 0.22	1.21 ± 0.12	18.8	200
12	59.5 ± 1.66	4.5 ± 0.21	28.0 ± 0.12	96.76 ± 3.48	2.73 ± 0.2	1.19 ± 0.1	18.4	201
1W	42 ± 1.35	5.3 ± 0.25	27.1 ± 0.1	72.58 ± 2.83	2.29 ± 0.15	1.08 ± 0.1	12.9	135
2W	60.5 ± 1.56	4.1 ± 0.21	27.1 ± 0.1	105.22 ± 3.5	2.96 ± 0.23	1.20 ± 0.11	19.1	209
$*$ (paraffin plus additives)	29 ± 0.13	3.5 ± 0.2	22.5 ± 0.05	72.93 ± 0.02	0.94 ± 0.13	2.26 ± 0.27	8.0	74
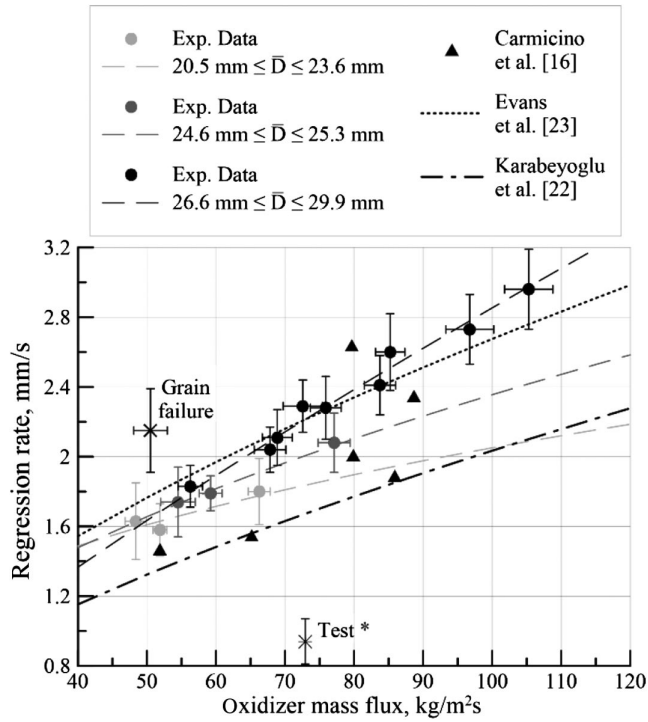
Fig. 4   Experimental fuel regression rate vs oxidizer mass flux and comparison with literature data and regression laws.

St_{0j}/St_0 accounts for the enhanced local heat transfer ensuing from the recirculation zone and the impingement of the oxidizer jet on the fuel surface with respect to the equivalent fully developed flow, whereas the ratio St_j/St_{0j} represents the heat transfer correction factor for the effects of wall blowing and combustion. Resorting to the data obtained in the separated, reattached, and redevelopment regions of circular tubes, the former term can be expressed in terms of the maximum heat transfer occurring in the region of reattachment as [5]

$$St_{0j}/St_0 = Re_D^{-0.2}(d_{inj}/D)^{-(2/3)} \qquad (12)$$

With substitution of Eq. (12), Eq. (10) can then be rearranged as follows:

$$\rho_f \dot{r}/G = 0.023 Re_D^{-0.4} Pr^{-(2/3)}(d_{inj}/D)^{-(2/3)}(St_j/St_{0j})B \qquad (13)$$

Equation (13) shows that, in hybrid rockets equipped with an axial injection configuration, unlike what was predicted under the hypothesis of turbulent boundary-layer flow, the grain port diameter explicitly influences regression rate for a given injector exit diameter.

In fact, in previous investigations [5,9], it has been proven that regression rate data, obtained with classical polymeric fuels burned with axially injected oxidizer, feature a clear dependency on the average port diameter; this phenomenon has been also reproduced by means of numerical simulations [19,27] and, because it is related to the convective heat transfer in the flow recirculation region, which increases with the port diameter at a given mass flux, it is reflected in the paraffin grain regression rate as well. However, because the regression rate of paraffin fuel grains is only partially governed by heat transfer to the wall, the phenomenon was still to be proven. As the position of the oxidizer attachment region on the grain surface (i.e., maximum heat transfer zone) depends on the distance from the injector exit section, the prechamber length has an influence on the regression rate, which is not considered in Eq. (13) because it was derived from the maximum heat transfer correlation. Anyway, in the present work, all the experimental tests have been carried out with the same configuration of the injector and of the prechamber, so that the dependency on those parameters disappears and the port diameter effect is properly investigated.

By correlating regression rate with oxygen mass flux and port diameter, the following relationship is obtained:

$$\bar{\dot{r}} = a\bar{G}_{ox}^n \bar{D}^m \qquad a = 0.029; \qquad n = 0.697;$$
$$m = 0.398 \quad (R^2 = 0.95) \qquad (14)$$

where the regression rate is expressed in millimeters per second, the mass flux is in kilograms per square meter second, and the port diameter is in millimeters. Also in this case, the data acquired in test 2 and test ∗ have been excluded from the correlation. It is worth noting that the value of the mass flux exponent in Eq. (14) is lower than the one in Eq. (9) and closer to that in Eq. (13); in particular, both the mass flux and the diameter exponents are close to the values predicted by Eq. (13). Moreover the exponents in Eq. (14) are in good agreement with those calculated on a larger motor burning pure HTPB and gaseous oxygen [9].

In Fig. 4, data obtained with the same motor burning paraffin grains casted with SEBS under N2O flow [16] are displayed for comparison. The average port diameter in the firing in these tests is almost constant to around 31–33 mm, which is comparable to the largest achieved in the current experimental campaign. Nevertheless, with the same levels of oxidizer mass flux, regression rate is lower than the one obtained with SASOL, and, as shown in Ref. [16], the different oxidizers do not play significant role. Thus, the slower regression of paraffin grains containing SEBS has to be attributed to the addition of polymers, once again confirming the key influence of the paraffin composition on the regression rate determination.

With larger port diameters, with the given discharge nozzle throat, higher chamber pressures are obtained (see Table 3). In this condition, one could correlate the data with oxygen mass flux and pressure as often found in the literature [5]. Specifically, considering tests characterized by intermediate oxidizer mass-flux values, different regression rates were observed for similar values of the oxidizer mass flux but relatively different pressures. In particular, tests 3 and 6 correspond to $\bar{G}_{ox}$ of about 67 kg/(m$^2 \cdot$ s) and pressures of 8.5 and 11.2 bar, respectively; tests 4 and 9 correspond to $\bar{G}_{ox}$ of about 76 kg/(m$^2 \cdot$ s) and pressures of 11.5 and 15.7 bar, respectively; and tests 10 and 11 correspond to $\bar{G}_{ox}$ of about 84 kg/(m$^2 \cdot$ s) and pressures of 16.9 and 18.8 bar, respectively.

A best-fit procedure gives the following correlation of the fuel regression rate as function of both the oxidizer mass flux and chamber pressure:

$$\bar{\dot{r}} = a\bar{G}_{ox}^n \bar{p}_c^m \qquad a = 0.157; \quad n = 0.51; \quad m = 0.17 \ (R^2 = 0.960) \qquad (15)$$

where, again, the regression rate is expressed in millimeters per second, the mass flux is in kilograms per square meter second, and the pressure is in bar.

From Eq. (3), by expressing the oxidizer mass flow rate in terms of the port area and mass flux, one obtains the following relationship for the chamber pressure:

$$p_c = \eta \frac{\pi}{4} G_{ox} \frac{D^2}{A_t}\left[\bar{C}^*\left(1 + \frac{1}{\overline{OF}}\right)\right] \qquad (16)$$

As tests were all performed with the same nozzle's throat area; by neglecting the variation of the term $\bar{C}^*(1 + 1/\overline{OF})$, which is essentially a function of the motor mixture ratio, chamber pressure is proportional to the oxidizer mass flux and the squared port diameter. Consequently, as pointed out in Ref. [5], also with the current set of data, the double of the pressure exponent in Eq. (15) is nearly equal to the diameter exponent in Eq. (14), and the sum of the power on pressure and the one on mass flux in Eq. (15) is very close to the mass flux exponent in Eq. (14). Thus, the diameter effect on the regression rate may induce an apparent pressure dependence, which can rather be disclosed only varying the nozzle throat over the tests.

Figure 5 shows the experimental time-averaged chamber pressure and thrust as functions of the oxidizer mass flow rate. For both
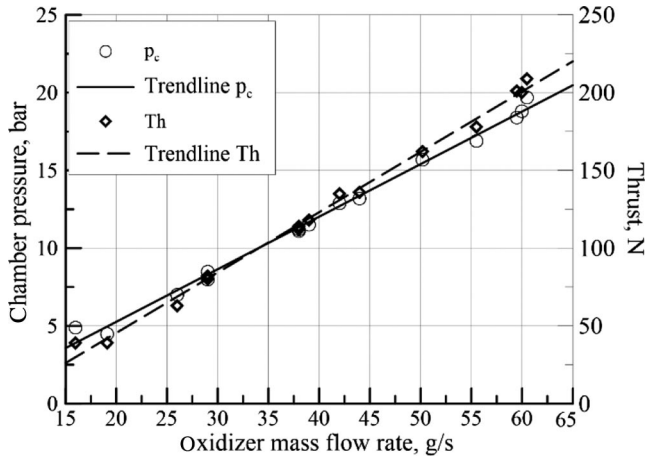
Fig. 5 Experimental average chamber pressure and thrust as functions of the oxidizer mass flow rate.

quantities, the trend is approximately linear in the considered interval.

IV. Numerical Simulation

The main purpose of the CFD simulations presented in this paper is the assessment of the combustion chamber flowfield and the calculation of pressure levels in pre- and postcombustion chambers for a comparison with the experimental data. Test 12 conditions have been considered; in this case, the chamber pressure is one of the largest among all the experimental tests, thus conditions are closer to those expected in the operation of the 1 kN future demonstrator.

In this framework, a common approach is the solution of the Reynolds-averaged Navier–Stokes (RANS) equations, with proper turbulence and combustion models. Moreover, because chemical and fluid-dynamic characteristic times are much shorter than the regression rate time scale, steady-state solution of RANS equations is dealt with [28]. A frequent simplifying practice is performing a single numerical simulation for the entire firing test considering the time-space-averaged port diameter [29].

Here, in analogy with Ref. [27], a simplified numerical model is used in which fuel regression rate is imposed decoupled from the flowfield; the effect of fuel mass addition is modeled considering gaseous fuel entering uniformly from the grain wall with an assigned mass flow rate. However, a combustion model different from the one in [27] is used among the ones suitable for nonpremixed flames.

A. Numerical Modeling Strategy

1. Governing Equations

The ANSYS Fluent ver. 16.0 commercial code was used for numerical simulations, adopting the pressure-based solver with the segregated SIMPLE algorithm.

Governing equations are reported next:

$$\frac{\partial \rho}{\partial t} + \frac{\partial}{\partial x_j}[\rho u_j] = 0 \qquad (17)$$

$$\frac{\partial}{\partial t}(\rho u_i) + \frac{\partial}{\partial x_j}[\rho u_i u_j + p\delta_{ij} - \tau_{ji}] = 0 \quad i = 1, 2, 3 \qquad (18)$$

$$\frac{\partial}{\partial t}(\rho e_0) + \frac{\partial}{\partial x_j}[\rho u_j e_0 + u_j p + q_j - u_i \tau_{ij}] = 0 \qquad (19)$$

where τ_{ij} represents the viscous stress:

$$\tau_{ij} = \mu \left(\frac{\partial u_i}{\partial x_j} + \frac{\partial u_j}{\partial x_i} - \frac{2}{3}\delta_{ij}\frac{\partial u_k}{\partial x_k} \right)$$

The heat flux q_j is given by Fourier's law:

$$q_j = -\lambda \frac{\partial T}{\partial x_j}$$

The total energy is defined by

$$e_0 = e + \frac{1}{2}u_k u_k + k$$

Note that the previous expression contains the extra term k, related to the turbulent energy.

Using segregated algorithm means that governing equations are solved sequentially (i.e., segregated from one another). Because the governing equations are nonlinear and coupled, the solution loop must be carried out iteratively to obtain a converged numerical solution, as illustrated in Fig. 6.

The SIMPLE algorithm, adopted in the performed simulations, uses a relationship between velocity and pressure corrections to enforce mass conservation and to obtain the pressure field. The complete mathematical dissertation can be found in [30]. The steady-state computation is second-order-accurate in space.

2. Thermodynamics and Transport Properties

Because of propellant inlet conditions, density is computed with the ideal gas equation of state for compressible flows:

$$\rho = \frac{p_{OP} + p}{(R/M_w)T} \qquad (20)$$

where p_{OP} represents the operating pressure, and p is the local relative (or gauge) pressure predicted by the solver.

The pure species heat capacities are defined by using the Fluent default piecewise polynomials, extracted from the Fluent properties database, in two temperature ranges (300–1000 and 1000–5000 K). The mixture's specific heat is computed as a mass fraction average of the pure species heat capacities with the following formula:
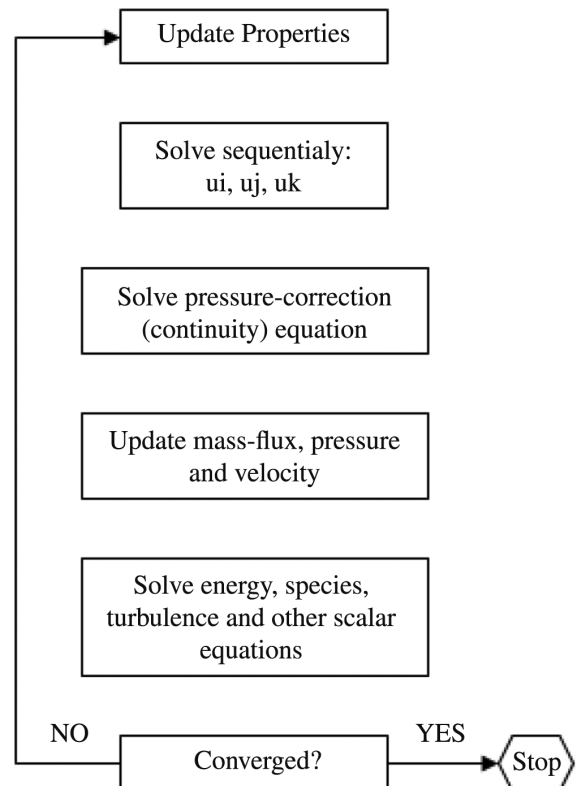

Fig. 6 Pressure-based segregated algorithm scheme as implemented in ANSYS Fluent [30].

$$c_p = \sum_i Y_i c_{p,i} \tag{21}$$

The pure species thermal conductivity is computed with the kinetic theory:

$$\lambda = \frac{15}{4} \frac{R}{M_w} \mu \left[\frac{4}{15} \frac{c_p M_w}{R} + \frac{1}{3} \right] \tag{22}$$

The mixture thermal conductivity is computed with the ideal-gas mixing law:

$$\lambda = \sum_i \frac{X_i \lambda_i}{\sum_j X_j \phi_{ij}} \tag{23}$$

where X_i is the mole fraction of species i, and

$$\phi_{ij} = \left[1 + \left(\frac{\mu_i}{\mu_j} \right)^{(1/2)} \left(\frac{M_{w,j}}{M_{w,i}} \right)^{(1/4)} \right]^2 \cdot \left[8 \left(1 + \frac{M_{w,i}}{M_{w,j}} \right) \right]^{-1/2}$$

where R is the universal gas constant, M_w is the molecular weight, μ is the viscosity, and c_p is the specific heat at constant pressure.

Also, the pure species viscosity is defined by adopting the kinetic theory, with the following law:

$$\mu = 2.67 \cdot 10^{-6} \frac{\sqrt{M_w T}}{\sigma^2 \Omega_\mu} \tag{24}$$

where $\Omega_\mu = \Omega_\mu(T^*)$ with $T^* = T/(\epsilon/k_B)$. The Lennard–Jones parameters σ and ϵ/k_B are set to 4 Å and 100 K, respectively. The mixture viscosity is computed with the ideal-gas mixing law as for thermal conductivity.

3. Turbulence Modeling

The shear-stress transport (SST) $k-\omega$ model, developed by Menter [31], was chosen for modeling turbulence. It is similar to the standard $k-\omega$ model but includes the addition of a cross-diffusion term in the ω equation and a blending function to ensure that the model equations behave appropriately in both the near-wall and far-field zones. The SST $k-\omega$ model has a similar form to the standard $k-\omega$ one:

$$\frac{\partial}{\partial t}(\rho k) + \frac{\partial}{\partial x_i}(\rho k u_i) = \frac{\partial}{\partial x_j}\left(\Gamma_k \frac{\partial k}{\partial x_j} \right) + \tilde{G}_k - Y_k + S_k \tag{25}$$

$$\frac{\partial}{\partial t}(\rho\omega) + \frac{\partial}{\partial x_i}(\rho\omega u_i) = \frac{\partial}{\partial x_j}\left(\Gamma_\omega \frac{\partial \omega}{\partial x_j} \right) + \tilde{G}_\omega - Y_\omega + D_\omega + S_\omega \tag{26}$$

where G_k represents the generation of turbulence kinetic energy due to mean velocity gradients; G_ω represents the generation of ω; Γ_k and Γ_ω represent the effective diffusivity of k and ω, respectively; Y_k and Y_ω represent the dissipation of k and ω due to turbulence; D_ω represents the cross-diffusion term; and S_k and S_ω are user-defined source terms.

4. Chemical Modeling

For the typical mass fluxes and operating pressures considered in the motor, fuel and oxidizer are assumed to be relatively slowly convected and mixed into the reaction zone, where they burn quickly, that is, the chemical kinetics is fast compared to the turbulent diffusion processes. Thus, the nonpremixed combustion of oxygen and gaseous products of paraffin wax vaporization (here the formation and entrainment of liquid droplets is neglected, i.e., fuel is supposed to enter the combustion chamber from the solid wall as a gaseous mixture of hydrogen and ethylene) is modeled with the eddy dissipation model as reported in Ref. [32] as well. The latter relies, indeed, on the hypothesis that the overall rate of reaction is controlled by turbulent mixing so that the unknown real chemical kinetic rates are expected to play a minor role and can be neglected.

Based on the work of Magnussen and Hjertager [33], the chemical reaction rate is governed by the large-eddy mixing time scale k/ϵ, as expressed in Eqs. (27) and (28), for which the net rate of production of species i due to reaction r, $R_{i,r}$, is given by the smaller (i.e., limiting value) of the two following equations:

$$R_{i,r} = \nu'_{i,r} M_{\omega,i} A \rho \frac{\epsilon}{k} \min_R \left(\frac{Y_R}{\nu'_{R,r} M_{\omega,R}} \right) \tag{27}$$

$$R_{i,r} = \nu'_{i,r} M_{\omega,i} A B \rho \frac{\epsilon}{k} \frac{\sum_P Y_P}{\sum_j^N \nu''_{j,r} M_{\omega,j}} \tag{28}$$

where Y_P is the mass fraction of any product species P, Y_R is the mass fraction of any product species R, and A and B are empirical constants equal to 4.0 and 0.5, respectively.

The adopted kinetic scheme considers a one-step reaction taking into account the most relevant species. In particular, CEA was used for the mixture calculation at the actual pressure and mixture ratio conditions, excluding species characterized by very low concentration. The resulting kinetic reaction is the following:

$$261 O_2 + 9 H_2 + 247 C_2 H_4 \rightleftharpoons 489 CO + 5 CO_2 + 8 H + 476 H_2 + 23 H_2 O$$
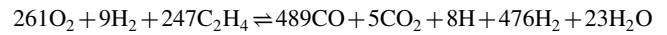
5. Computational Grids and Boundary Conditions

Three-dimensional simulations were carried out adopting different nonstructured grids which are shown in Fig. 7, with three levels of refinement, as reported in Table 4, considering a computational domain made of a 60 deg wedge with periodic conditions imposed to the lateral planes. The computational domain was generated by considering the time-space-averaged port diameter in the burning.

With all the grids characterized by the same height value of the first cell at wall, $y+$ are about the same in all the cases, except in the nozzle throat, where some differences can be discerned between the medium/fine and the coarse grid levels. Considering the prechamber region, $y+$ is between 0 and 10. In the postchamber, $y+$ assumes values between 20 and 30, whereas in the nozzle throat, the highest value is about 130 for the medium and fine mesh predictions. All these values are suitable with the adopted automatic wall treatment of the $k-\omega$ SST model, thus allowing a correct estimation of wall heat fluxes.

The boundary conditions imposed mass-flow inlet for both oxygen and paraffin wax (C_2H_4 and H_2), with values derived by the experimental firing test conditions (test 12). Specifically, the oxygen mass flow was constant during the firing test, and the fuel mass flow rate was imposed based on the port diameter and average regression rate. The imposed values are reported in Table 5.

Isothermal chamber walls at 300 K and pressure outlet at ambient pressure and temperature were assumed.
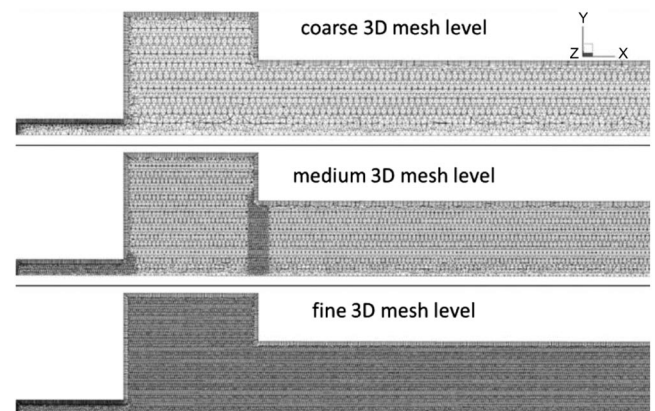

Fig. 7 Computational meshes.

Table 4 Main characteristics of the computing mesh

Parameter	Coarse level	Medium level	Fine level
Number of cells	~250,000	~1,200,000	~5,000,000
First wall cell height, m	1e-5	1e-5	1e-5
Mesh quality	>0.6 for 99% of cells	>0.6 for 99% of cells	>0.6 for 99% of cells

Table 5 Imposed boundary conditions (test 12)

Species	Mass flow inlet, kg/s	Temperature, K
Oxygen (O_2)	0.0595	300
Paraffin ($0.997C_2H_4 + 0.003H_2$)[a]	0.0496	725

[a]Gas composition at the fuel wall by mass fraction.

B. Results

The temperature field across the whole computational domain is depicted in Fig. 8, by means of both flood and isolines, in the midplane volume slice extracted from the three meshes. Considering the solution obtained on the fine mesh level (see the image on the bottom), the reaction occurs in proximity of the injector exit, where temperature values rapidly increase, then it proceeds all over the grain surface and reaches the postchamber, where the highest temperature values are expected. By comparing solutions obtained with the three different grid levels, it is clear that the field obtained with the coarse mesh is substantially different from the medium and fine grid refinements. In particular, temperatures in the prechamber region are very high, whereas the initial portion of the propellant grain is characterized by lower temperatures. On the other hand, both the medium and the fine mesh levels produce a forward shift of the reaction zone in proximity of the grain, with higher uniformity in the fine mesh solution. Considering the postchamber and nozzle regions, solutions associated with medium and fine mesh levels are in very good agreement with each other. In the prechamber region, increasing the mesh level leads to decreasing the predicted temperatures.

Figure 9 shows the predicted velocity stream traces, colored with temperature extracted from the fine-mesh solution. In agreement with Refs. [19,27,28], a clear main recirculating bubble is predicted that extends from the prechamber up to the solid grain port, carrying gaseous fuel from the grain back in this region. Temperature values show that, because of the presence of both oxygen and fuel, the reaction occurs in proximity of the injector exit. In the prechamber region, temperature values are below 800 K.

Postfiring test visual inspection revealed, also in the case of [16], the presence of paraffin wax in the prechamber region and on the motor head hand flange, which is an evidence of what numerically predicted.
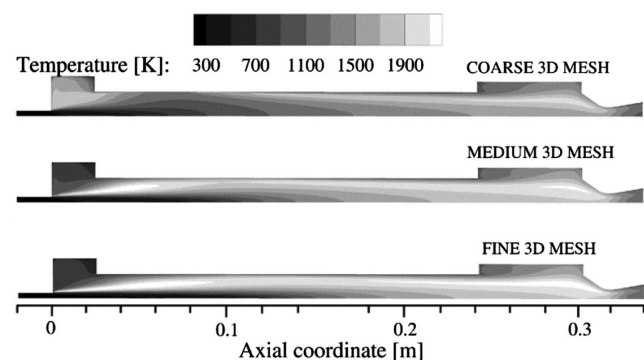
Figure 10 shows the temperature profiles extracted along the line highlighted in the small frame in the picture, which is located at half postchamber ($X = 0.28$ m).

The predicted temperature peak value is about 2160 K with the fine mesh, about 2080 K with the medium, and 1940 K with the coarse one, meaning that increasing the mesh level leads to increasing the temperature peak value. Considering the average values along the extracted line, results are consistent with the prediction given by CEA, in chemical equilibrium under the same pressure and mixture ratio conditions. Specifically, CEA indicates an average temperature value equal to 1780 K. Quantitative values are reported in Table 6 and show that the deviation from the CEA prediction is 11.8% for the coarse mesh, 1.8% for the medium, and 0.4% for the fine one, considering the average quantities.

Figure 11 shows the predicted wall heat flux over the prechamber wall. A good solution convergence is well visible, with differences between predictions with medium and fine levels much smaller than those associated by adopting coarse and medium levels. Heat-flux value does not exceed 0.2 MW/m² for the prediction on the more refined mesh. This value increases to about 0.25 MW/m², considering the medium mesh prediction and to 0.95 MW/m² on the coarse level.

Concerning the postchamber (see Fig. 12), numerical predictions show a heat-flux distribution almost flat. Considerations similar to the prechamber can be made about the solution dependence on the mesh. In particular, a good agreement is found between predictions associated with the medium and the fine grid levels, with highest values approaching about 1.8 MW/m². In this case, lower heat fluxes are predicted by the coarse mesh (about 1.5 MW/m²) because temperature values in this region are lower in this case, as previously discussed.

Figures 13 and 14 show heat-flux distributions over the motor forward flange and the nozzle wall, respectively. For both cases,
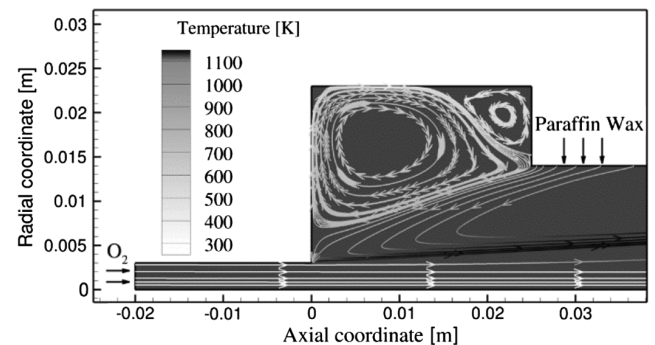
Fig. 9 Temperature contour plot and velocity stream trace colored with temperature extracted from the fine-mesh solution.
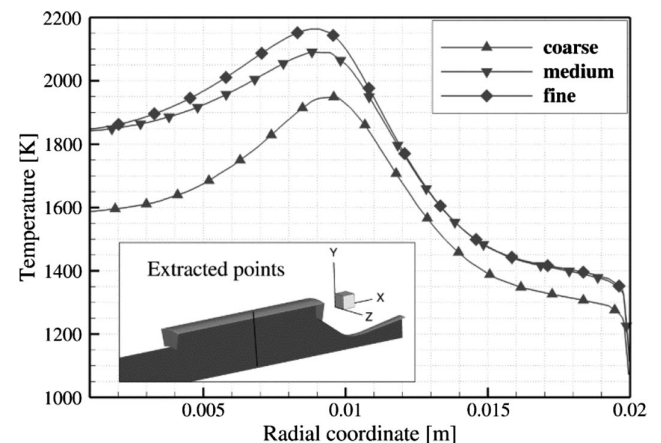
Fig. 8 Computed temperature contour plots over the midplane volume slice for the different meshes.

Fig. 10 Temperature profile along the half postchamber vertical line.

Table 6 Predicted temperatures in the half postchamber extractions

Parameter	Coarse mesh	Medium mesh	Fine mesh
T peak, K	1940	2080	2160
T average, K	1592.2	1748.6	1772.6
T REF-CEA, K	1780	1780	1780
Deviation, %	11.8	1.8	0.4

a very good solution convergence is visible, as found also for the predictions over the pre- and postchamber. In particular, heat flux over the flange is characterized by an almost flat distribution, with average values approaching about 0.4 and 0.3 MW/m² for the medium and fine mesh levels, respectively. Heat-flux distributions in the nozzle show the typical peak in proximity of the throat, with peak values of about 12.5 MW/m² for both the medium and fine mesh predictions.

The main numerical results predicted for the simulated test 12 are summarized in Table 7, where the predicted average heat-flux values on the walls and the corresponding peak value in the nozzle are reported.

Figure 15 shows a log-log plot of the numerical error versus the grid size for the average quantities computed in the postchamber, reported in Tables 6 and 7. Spatial convergence study is carried out determining the discretization error of the CFD simulations according to the methods presented in [34]. The numerical error of a given parameter corresponding to each computational grid

(coarse, medium, and fine) has been evaluated as the relative difference between the computed value and the relevant Richardson extrapolation.

Chamber pressure was experimentally measured in both pre- (PT1) and postchamber (PT2) (see Fig. 2) during the firing test, detecting an average value of 18.9 bar of PT1 (±0.53 bar) and 18.4 bar of PT2 (±0.46 bar). The numerical estimation obtained on the medium and fine mesh levels is quite similar, as can be seen in the plot of Fig. 16, where the pressure distribution along the motor axis is reported, together with the two values experimentally measured.

Specifically, as expected from the combined effects of the mass addition and heat transfer [35], the numerical trends show that pressure slightly decreases from the injector up to the discharge nozzle, approaching average values between 18.2 (medium mesh) and 18.3 bar (fine mesh), which correspond to deviations from the experimental values equal to about 4% (with respect to PT1) and 1% (with respect to PT2) in the worst case, respectively.

The numerical pressure value associated with the coarse mesh is about 17.5 bar, showing an underestimation with respect to values predicted by the more refined meshes. In this case, the deviation from the experimental values is about 8% considering PT1 and 5% considering PT2. It is worth noting that refining the mesh leads to increasing the estimated chamber pressure. Comparing coarse, medium, and fine predictions, a numerical convergence can be deduced, with the difference between values predicted by the coarse and medium levels equal to 4% and the difference between values predicted by the medium and fine levels equal to 0.5%.
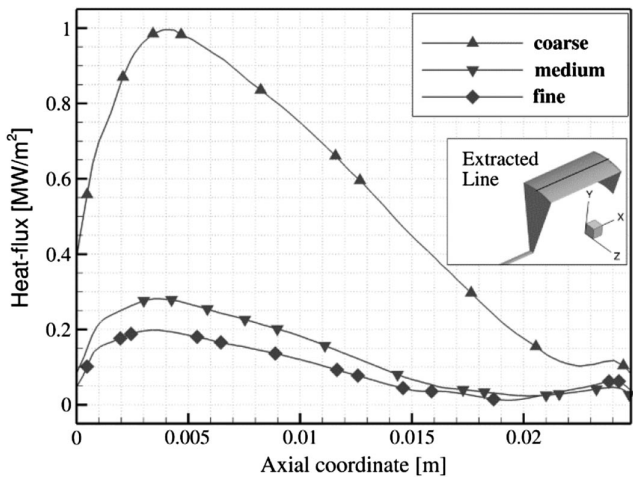

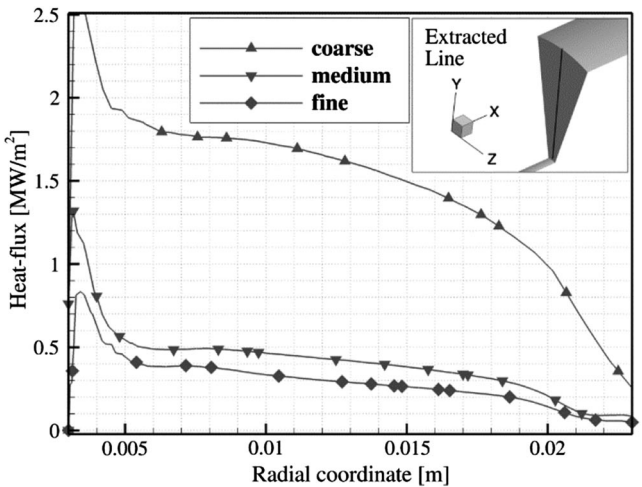Fig. 11 Heat-flux distribution over the prechamber wall.

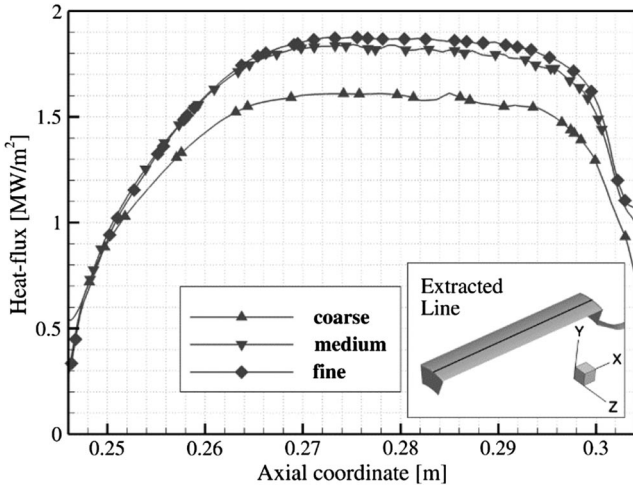Fig. 13 Heat-flux distribution over the motor head flange.

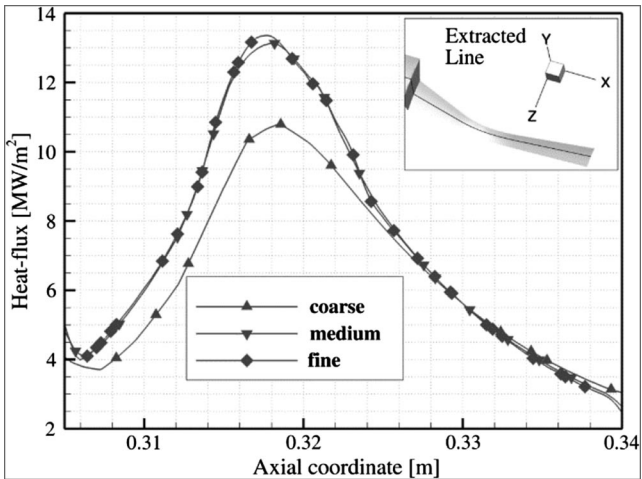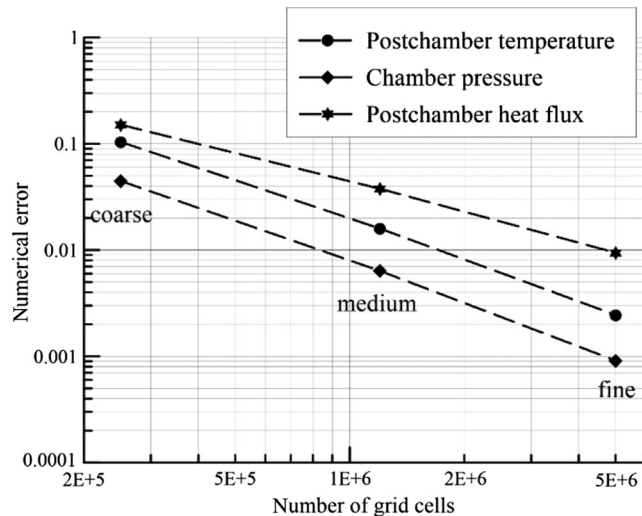Fig. 12 Heat-flux distribution over the postchamber wall.

Fig. 14 Heat-flux distribution over the nozzle wall.

Table 7   Main numerical results predicted for test 12

Grid refinement	Chamber pressure, bar	Head flange heat flux, MW/m²	Prechamber heat flux, MW/m²	Postchamber heat flux, MW/m²	Nozzle heat flux, MW/m²
Coarse	17.5	1.40	0.55	1.50	10.2
Medium	18.2	0.40	0.15	1.70	12.5
Fine	18.3	0.30	0.10	1.75	12.5

Fig. 15   Numerical error vs grid size.
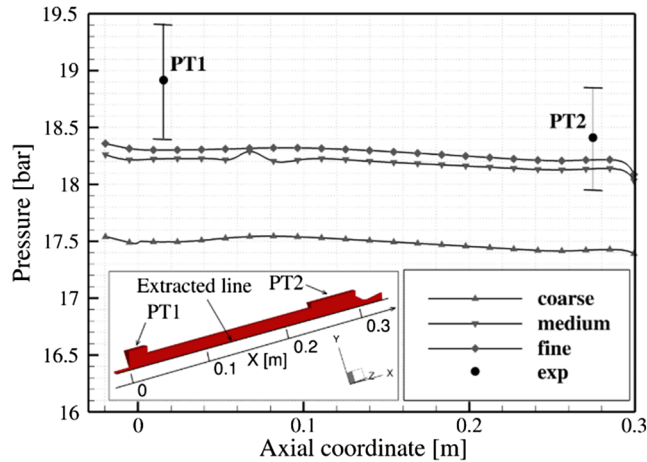
Fig. 16   Chamber pressure numerically predicted along the motor axis and experimentally measured.

V.   Conclusions

With the long-term target of designing, manufacturing, and testing a 1 kN hybrid rocket demonstrator fed by oxygen and paraffin wax fuel, preliminary firings were carried out on a subscale rocket motor for investigating basic aspects, including paraffin wax characterization.

Seventeen firing tests were performed at several oxidizer mass fluxes using the SASOL-0907 paraffin-based fuel. Results showed that the selected paraffin fuel allows for good performance while guaranteeing the necessary structural strength under the experimented test conditions, which ranged up to 20 bar combustion pressure and over a wide interval of mixture ratios. In all the experimental tests, no grain failures occurred, except for only one test, which was probably related to axial loads deriving from a wrong assembly. The measured regression rate was found to be fairly aligned with some trends in the literature but showing a dependence on the port diameter other than on

the mass flux. This behavior can be attributed to the effect of the flow recirculation generated at the engine head end due to the axial injection of the oxidizer, similar to what has been found in previous work with polymeric fuels. The effects of the recirculation generated by the nozzle injector are demonstrated also by the significant paraffin slivers found after the firings on the motor injection flange and prechamber wall, in the cases where the motor overall mixture ratio was particularly low.

Experimental work was supported and complemented by numerical simulations. The adopted numerical modeling strategy allowed estimating chamber pressure values in line with those experimentally measured. Moreover, a recirculating bubble at the injector exit was numerically predicted, and it is responsible for carrying back paraffin wax in the prechamber region. The validation of the numerical model allows exploiting all the additional results provided by the computations, such as the temperature distribution inside the motor and the heat fluxes expected on the prechamber, postchamber, and nozzle walls, which are very useful for the design and optimization of the larger-scale hybrid rocket demonstrator.

References

[1] Altman, D., and Holzman, A., "Overview and History of Hybrid Rocket Propulsion," *Fundamentals of Hybrid Rocket Combustion and Propulsion*, edited by K. Kuo, and M. Chiaverini, Vol. 218, Progress in Astronautics and Aeronautics, AIAA, Reston, VA, 2007, pp. 1–36.
doi:10.2514/5.9781600866876.0001.0036

[2] Altman, D., and Humble, R., "Hybrid Rocket Propulsion Systems," *Space Propulsion Analysis and Design*, edited by R. W. Humble, G. N. Henry, and W. J. Larson, 1st ed., McGraw–Hill, New York, 1995, pp. 365–370.

[3] Sutton, G. P., and Biblarz, O., "Hybrid Propellant Rockets," *Rocket Propulsion Elements*, 7th ed., Wiley, New York, 2001, pp. 585–593.

[4] Marxman, G. A., and Gilbert, M., "Turbulent Boundary Layer Combustion in the Hybrid Rocket," *Symposium (International) on Combustion*, Vol. 9, No. 1, 1963, pp. 371–383.
doi:10.1016/S0082-0784(63)80046-6

[5] Carmicino, C., and Russo Sorge, A., "Role of Injection in Hybrid Rockets Regression Rate Behavior," *Journal of Propulsion and Power*, Vol. 21, No. 4, 2005, pp. 606–612.
doi:10.2514/1.9945

[6] Carmicino, C., and Russo Sorge, A., "Influence of a Conical Axial Injector on Hybrid Rocket Performance," *Journal of Propulsion and Power*, Vol. 22, No. 5, 2006, pp. 984–995.
doi:10.2514/1.19528

[7] Motoe, M., and Shimada, T., "Numerical Simulations of Combustive Flows in a Swirling-Oxidizer-Flow-Type Hybrid Rocket," *52nd Aerospace Sciences Meeting*, AIAA Paper 2014-0310, 2014.
doi:–10.2514/6.2014–0310

[8] Kumar, C. P., and Kumar, A., "A Numerical Study on the Regression Rate of Hybrid Rocket Motors Using a Combination of Enhancement Techniques," *48th AIAA/ASME/SAE/ASEE Joint Propulsion Conference & Exhibit*, AIAA Paper 2012-4105, July–Aug. 2012.
doi:10.2514/6.2012-4105

[9] Carmicino, C., and Russo Sorge, A., "Experimental Investigation into the Effect of Solid-Fuel Additives on Hybrid Rocket Performance," *Journal of Propulsion and Power*, Vol. 31, No. 2, 2015, pp. 699–713.
doi:10.2514/1.B35383

[10] Karabeyoglu, M. A., Cantwell, B. J., and Altman, D., "Development and Testing of Paraffin-Based Hybrid Rocket Fuels," *37th Joint Propulsion Conference and Exhibit*, AIAA Paper 2001-4503, July 2001.
doi:10.2514/6.2001-4503

[11] Mazzetti, A., Merotto, L., and Pinarello, G., "Paraffin-Based Hybrid Rocket Engines Applications: A Review and a Market Perspective," *Acta Astronautica*, Vol. 126, Sept.–Oct. 2016, pp. 286–297.
doi:10.1016/j.actaastro.2016.04.036

[12] Chandler, A., Jens, E., Cantwell, B. J., and Hubbard, G. S., "Visualization of the Liquid Layer Combustion of Paraffin Fuel for Hybrid Rocket Applications," *48th AIAA/ASME/SAE/ASEE Joint Propulsion Conference*

& *Exhibit*, AIAA Paper 2012-3961, July–Aug. 2012.
doi:10.2514/6.2012-3961

[13] Petrarolo, A., and Kobald, M., "Evaluation Techniques for Optical Analysis of Hybrid Rocket Propulsion," *Journal of Fluid Science and Technology*, Vol. 11, No. 4, 2016, Paper JFST0028.
doi:10.1299/jfst.2016jfst0028

[14] Kobald, M., Schmierer, C., Ciezki, H. K., Schlechtriem, S., Toson, E., and De Luca, L. T., "Viscosity and Regression Rate of Liquefying Hybrid Rocket Fuels," *Journal of Propulsion and Power*, Vol. 33, No. 5, 2017, pp. 1245–1251.
doi:10.2514/1.B36207

[15] Veale, K., Adali, S., Pitot, J., and Brooks, M., "A Review of the Performance and Structural Considerations of Paraffin Wax Hybrid Rocket Fuels with Additives," *Acta Astronautica*, Vol. 141, Dec. 2017, pp. 196–208.
doi:10.1016/j.actaastro.2017.10.012

[16] Carmicino, C., Scaramuzzino, F., and Russo Sorge, A., "Trade-Off Between Paraffin-Based and Aluminium-Loaded HTPB Fuels to Improve Performance of Hybrid Rocket Fed with N_2O," *Aerospace Science and Technology*, Vol. 37, Aug. 2014, pp. 81–92.
doi:10.1016/j.ast.2014.05.010

[17] Marxman, G. A., "Combustion in the Turbulent Boundary Layer on a Vaporizing Surface," *Symposium (International) on Combustion*, Vol. 10, No. 1, 1965, pp. 1337–1349.
doi:10.1016/S0082-0784(65)80268-5

[18] Karabeyoglu, M. A., Altman, D., and Cantwell, B. J., "Combustion of Liquefying Hybrid Propellants: Part 1, General Theory," *Journal of Propulsion and Power*, Vol. 18, No. 3, 2002, pp. 610–620.
doi:10.2514/2.5975

[19] Bianchi, D., Nasuti, F., and Carmicino, C., "Hybrid Rockets with Axial Injector: Port Diameter Effect on Fuel Regression Rate," *Journal of Propulsion and Power*, Vol. 32, No. 4, 2016, pp. 984–996.
doi:10.2514/1.B36000

[20] George, P., Krishnan, S., Varkey, P. M., Ravindran, M., and Ramachandran, L., "Fuel Regression Rate in Hydroxyl-Terminated-Polybutadiene/Gaseous-Oxygen Hybrid Rocket Motors," *Journal of Propulsion and Power*, Vol. 17, No. 1, 2001, pp. 35–42.
doi:10.2514/2.5704

[21] Price, C. F., and Smoot, L. D., "Regression Rates of Nonmetalized Hybrid Fuel Systems," *AIAA Journal*, Vol. 3, No. 8, 1965, pp. 1408–1413.
doi:10.2514/3.3160

[22] Saccone, G., Piscitelli, F., Gianvito, A., Cosentino, G., and Mazzola, L., "Manufacturing Processes of Paraffin Grains as Fuel for Hybrid Rocket Engines," *51st AIAA/SAE/ASEE Joint Propulsion Conference*, AIAA Paper 2015-4039, July 2015.
doi:10.2514/6.2015-4039

[23] Kobald, M., Toson, E., Ciezki, H., Schlechtriem, S., di Betta, S., Coppola, M., and De Luca, L., "Rheological, Optical, and Ballistic Investigations of Paraffin-Based Fuels for Hybrid Rocket Propulsion Using a Two-Dimensional Slub-Burner," *Progress in Propulsion Physics*, Vol. 8, July 2016, pp. 263–282.
doi:10.1051/eucass/201608263

[24] Karabeyoglu, A., Zilliac, G., Cantwell, B. J., De Zilwa, S., and Castellucci, P., "Scale-Up Tests of High Regression Rate Paraffin-Based Hybrid Rocket Fuels," *Journal of Propulsion and Power*, Vol. 20, No. 6, 2004, pp. 1037–1045.
doi:10.2514/1.3340

[25] Evans, B., Favorito, A., and Kuo, K., "Study of Solid Fuel Burning-Rate Enhancement Behavior in an X-Ray Translucent Hybrid Rocket Motor," *41st AIAA/ASME/SAE/ASEE Joint Propulsion Conference & Exhibit*, AIAA Paper 2005-3909, July 2005.
doi:10.2514/6.2005-3909

[26] Gordon, S., and McBride, B. J., "Computer Program of Complex Chemical Equilibrium Compositions and Applications," NASA RP-1311, Oct. 1994.

[27] Di Martino, G. D., Malgieri, P., Carmicino, C., and Savino, R., "A Simplified Computational Fluid-Dynamic Approach to the Oxidizer Injector Design in Hybrid Rockets," *Acta Astronautica*, Vol. 129, Dec. 2016, pp. 8–21.
doi:10.1016/j.actaastro.2016.08.026

[28] Di Martino, G. D., Carmicino, C., and Savino, R., "Transient Computational Thermofluid-Dynamic Simulation of Hybrid Rocket Internal Ballistics," *Journal of Propulsion and Power*, Vol. 33, No. 6, 2017, pp. 1395–1409.
doi:10.2514/1.B36425

[29] Bianchi, D., Betti, B., Nasuti, F., and Carmicino, C., "Simulation of Gaseous Oxygen/Hydroxyl-Terminated Polybutadiene Hybrid Rocket Flowfields and Comparison with Experiments," *Journal of Propulsion and Power*, Vol. 31, No. 3, 2015, pp. 919–929.
doi:10.2514/1.B35587

[30] *ANSYS FLUENT Theory Guide-Release 15.0*, Ansys Inc., Canonsburg, PA, Nov. 2013.

[31] Menter, F. R., "Two-Equation Eddy-Viscosity Turbulence Models for Engineering Applications," *AIAA Journal*, Vol. 32, No. 8, 1994, pp. 1598–1605.
doi:10.2514/3.12149

[32] Lazzarin, M., Faenza, M., Barato, F., and Bellomo, N., "CFD Simulation of a Hybrid Rocket Motor with Liquid Injection," *47th AIAA/ASME/SAE/ASEE Joint Propulsion Conference & Exhibit*, AIAA Paper 2011-5537, July–Aug. 2011.
doi:10.2514/6.2011-5537

[33] Magnussen, B. F., and Hjertager, B. H., "On Mathematical Models of Turbulent Combustion with Special Emphasis on Soot Formation and Combustion," *Symposium (International) on Combustion*, Vol. 16, No. 1, 1977, pp. 719–729.
doi:10.1016/S0082-0784(77)80366-4

[34] Roache, P. J., *Verification and Validation in Computational Science and Engineering*, Hermosa Publishers, Albuquerque, NM, 1998, pp. 403–412.

[35] Carmicino, C., and Pastrone, D., "Novel Comprehensive Technique for Hybrid Rockets Experimental Ballistic Data Reconstruction," *Journal of Propulsion and Power*, Vol. 34, No. 1, 2018, pp. 133–145.
doi:10.2514/1.B36517

J. C. Oefelein
Associate Editor